

1  
2  
3  
4  
5  
6  
7  
8  
9  
10  
11  
12  
13  
14  
15  
16  
17  
18  
19  
20  
21  
22  
23  
24  
25  
26  
27

## **MJO Propagation Processes and Mean Biases in the SubX and S2S Reforecasts**

Hyemi Kim<sup>1</sup>, Matthew A. Janiga<sup>2</sup>, and Kathy Pegion<sup>3</sup>

<sup>1</sup>School of Marine and Atmospheric Sciences, Stony Brook University, Stony Brook, NY

<sup>2</sup>Naval Research Laboratory, Marine Meteorology Division, Monterey, CA

<sup>3</sup>Department of Atmospheric, Oceanic and Earth Sciences, George Mason University, Fairfax,  
VA

### **J. Geophysical Research - Atmospheres**

*(Special section: Bridging Weather and Climate: Subseasonal-to-Seasonal (S2S) Prediction)*

#### **Key Points:**

- SubX and S2S reforecasts show MJO prediction skill out to 4.5 weeks based on the RMM index.
- SubX and S2S models fail to predict the MJO convection, associated circulations, and moisture advection processes beyond 10 days.
- SubX and S2S models have mean biases across the Indo-Pacific: a drier low troposphere, excess of surface precipitation, frequent occurrence of light precipitation.

\* Corresponding author:

Hyemi Kim ([hyemi.kim@stonybrook.edu](mailto:hyemi.kim@stonybrook.edu))

119 Endeavor Hall, School of Marine and Atmospheric Sciences, Stony Brook University, Stony Brook, NY, 11794-5000, USA

28  
29  
30  
31  
32  
33  
34  
35  
36  
37  
38  
39  
40  
41  
42  
43  
44  
45  
46

**Abstract**

The Madden-Julian Oscillation (MJO) is the leading source of global subseasonal predictability; however, many dynamical forecasting systems struggle to predict MJO propagation through the Maritime Continent (MC). Better understanding the biases in simulated physical processes associated with MJO propagation is the key to improve MJO prediction. In this study, MJO prediction skill, propagation processes, and mean state biases are evaluated in reforecasts from models participating in the Subseasonal Experiment (SubX) and Subseasonal to Seasonal (S2S) prediction projects. SubX and S2S reforecasts show MJO prediction skill out to 4.5 weeks based on the Real-time Multivariate MJO (RMM) index consistent with previous studies. However, a closer examination of these models' representation of MJO propagation through the MC reveals that they fail to predict the MJO convection, associated circulations, and moisture advection processes beyond 10 days with most of models underestimating MJO amplitude. The biases in the MJO propagation can be partly associated with the following mean biases across the Indo-Pacific: a drier low troposphere, excess surface precipitation, more frequent occurrence of light precipitation rates, and a transition to stronger precipitation rates at lower humidity than in observations. This indicates that deep convection occurs too frequently in models and is not sufficiently inhibited when tropospheric moisture is low, which is likely due to the representation of entrainment.

47 **1. Introduction**

48 The Madden-Julian Oscillation (MJO, Madden and Julian 1971, 1972) is the leading source  
49 of global subseasonal predictability. There have been enormous advances in MJO prediction in  
50 the last decade; leading dynamical forecasting systems are skillful out to five weeks (e.g., review  
51 by Kim et al. 2018). Several internationally coordinated multi-model reforecast experiments  
52 have made such advances possible. For example, the World Weather Research  
53 Programme/World Climate Research Programme Sub-seasonal to Seasonal Prediction project  
54 (hereafter S2S project, Vitart et al. 2017) was launched in 2013 and provides both near real-time  
55 and a long record (> 10 years) of extended-range (up to 60 days) forecasts from operational  
56 centers with the aim of better understanding global subseasonal predictability and its translation  
57 into useful forecast information. Many S2S project models have demonstrated improved MJO  
58 prediction compared to their earlier versions (e.g., Vitart 2017, Lim et al. 2018). Another newly  
59 launched Subseasonal Experiment (SubX, Kirtman et al. 2017), which is a National Oceanic and  
60 Atmospheric Administration (NOAA) Climate Testbed project, consists of multi-models from  
61 the current generation prediction systems by multi-agencies from North America, such as the  
62 NOAA, National Aeronautics and Space Administration (NASA), and Naval Research Lab  
63 (NRL). The SubX project produces real-time forecasts as well as reforecasts going back to 1999.  
64 MJO prediction skill in SubX models is comparable to those from the S2S project (Janiga et al.  
65 2018; Pegion et al. 2019). These ongoing internationally coordinated efforts on subseasonal  
66 prediction provide an unprecedented opportunity to further understand the predictability of the  
67 MJO.

68 Although studies have shown continuous improvements in MJO prediction in the past  
69 decade, simulation of MJO eastward propagation, particularly across the Maritime Continent

70 (MC), remains a challenge. When the MJO propagates eastward from the Indian Ocean to the  
71 western Pacific, it is often disrupted by the MC due to orography and diurnal convection; this is  
72 referred to as the MC barrier effect (e.g., review by Kim et al. 2019). This MC barrier effect is  
73 exaggerated in dynamical forecasting systems; the percentage of MJO events not crossing the  
74 MC is significantly higher in forecasts than in observations indicating the inability of models to  
75 maintain MJO propagation through the MC (Neena et al. 2014; Kim et al. 2014, 2018; Wang et  
76 al. 2014; Xiang et al. 2015; Liu et al. 2017; Vitart 2017; Wang et al. 2018). Better understanding  
77 of the sources of model errors in MJO propagation processes is crucial for improving MJO  
78 prediction skill.

79       Recent theoretical, observational, and modeling studies demonstrate that the propagation of  
80 the MJO is tightly linked to the seasonal mean state. Predicated on the moisture mode framework  
81 (e.g., Raymond and Fuchs 2009; Sobel and Maloney 2012, 2013; Adames and Kim 2016), it has  
82 been argued that the advection of the low-tropospheric seasonal mean moisture by the MJO  
83 associated circulation anomalies plays an important role in the eastward propagation of the MJO  
84 through the MC (Jiang et al. 2015, 2018; Adames and Kim 2016; Jiang 2017; Kim et al. 2019).  
85 Specifically, the horizontal gradient of the mean moisture determines the magnitude of the  
86 moistening (drying) to the east (west) of the enhanced MJO, thereby enabling or disabling the  
87 eastward propagation. In global climate models (GCMs), mean biases develop quickly within a  
88 week in the tropics (e.g., Janiga et al. 2018) and can distort the MJO simulation and prediction  
89 by influencing further development of the MJO and its interaction with the mean state (Gonzalez  
90 and Jiang 2017; Jiang 2017; Kim 2017; Lim et al. 2018). Kim (2017) found that the predicted  
91 MJO amplitude rapidly becomes weaker than the observed amplitude when it propagates across  
92 the MC in the European Centre for Medium-Range Weather Forecasts (ECMWF) model. The

93 weak MJO in the model is mostly attributed to reduced horizontal moisture advection which is  
94 partly caused by the dry bias in the low-tropospheric seasonal mean moisture. Consistent results  
95 are found with S2S project models by Lim et al. (2018) which shows that models with smaller  
96 biases in the mean moisture gradient tend to have higher MJO prediction skill. However, a lack  
97 of detailed analysis of MJO propagation processes in Lim et al. (2018) and the use of a single  
98 model in Kim (2017) motivate further research on the relationship between MJO prediction skill,  
99 MJO propagation processes, and mean state biases in a diverse set of models.

100 Better understanding the sources of errors in MJO processes is the key to improving MJO  
101 prediction. Process-based diagnostics aim to ascertain which physical processes should be  
102 targeted for improvement in models to better simulate the MJO and help focus model  
103 development efforts (e.g., review by Jiang et al. 2019; Maloney et al. 2019). However, process-  
104 based model evaluations of MJO prediction are limited in number and largely limited to case  
105 studies of individual MJO events (Ling et al. 2014; Hannah and Maloney 2014; Hannah et al.  
106 2015; Klingaman et al. 2015). The SubX and S2S projects, which make available a large number  
107 of ensemble forecasts of numerous fields covering multiple years from current dynamical  
108 prediction systems, provide an opportunity to conduct a thorough process-based study of MJO  
109 prediction. The process-based approach in this study sheds light on which physical processes in  
110 the dynamical models, especially in the cumulus parameterization, needs to be better represented  
111 to further improve MJO prediction. The SubX and S2S reforecasts and validation data sets are  
112 introduced in section 2. MJO prediction skill, amplitude and phase biases are assessed in section  
113 3. MJO propagation processes and mean state biases are discussed in section 4, followed by  
114 summary and discussion in section 5.

115

116 **2. Data and method**

117 Reforecasts from the SubX project include the National Centers for Environmental  
118 Prediction Environmental Modeling Center Global Ensemble Forecast System (NCEP-GEFS),  
119 NASA Global Modeling and Assimilation Office Goddard Earth Observing System (NASA-  
120 GEOS5), Naval Research Laboratory Navy Earth System Prediction Capability (Navy-ESPC),  
121 National Center for Atmospheric Research (NCAR) Community Climate System Model version  
122 4 run at the University of Miami Rosenstiel School for Marine and Atmospheric Science  
123 (RSMAS-CCSM4), and NOAA Earth System Research Laboratory Flow-Following Icosahedral  
124 Model (ESRL-FIM). In addition to these five SubX models, NCAR Community Earth System  
125 Model version 1 (NCAR-CESM1) reforecasts with two different vertical levels (L30 and L46)  
126 are compared. Because of the comparable MJO simulation characteristics and prediction skill in  
127 L30 and L46, we combine them into a 20-member ensemble of 10 members each. Two models  
128 from the S2S project, ECMWF version CY43R3 (ECMWF-CY43R3) and Korea Meteorological  
129 Administration-UK Met Office coupled Global Seasonal forecast (KMA-GloSea5), are  
130 evaluated. Those two S2S project models are chosen due to their relatively high MJO prediction  
131 skill (Lim et al. 2018). The ECMWF-CY43R3 version is the most updated version which  
132 consists of 20-year reforecasts. All models have fully coupled atmosphere-ocean-land-sea ice  
133 models, except the NCEP-GEFS which is forced by prescribed sea surface temperature (SST)  
134 from the operational NCEP Climate Forecast System v2 (Pegion et al. 2019). Ensemble sizes,  
135 reforecast periods, and initialization intervals in eight reforecasts are compared in Table 1.  
136 Readers are referred to Vitart et al. (2017) and Pegion et al. (2019) for a more detailed  
137 description of each model configurations. All models have reforecasts out to a minimum of 32  
138 days. The results shown in this study are from the ensemble mean unless otherwise stated.

139 ECMWF Reanalysis Interim (ERA-interim, Dee et al. 2011), NOAA Advanced Very High-  
140 Resolution Radiometer (Liebmann and Smith 1996) Outgoing Longwave Radiation (OLR)  
141 product from 1979 to 2017, and Global Precipitation Climatology Project 1° daily version 1.2  
142 (GPCP-1DD, Huffman et al. 2001) from 1997 to 2015 are compared with the reforecasts. We  
143 refer to these datasets as observations for simplicity. All observations and reforecasts are  
144 interpolated to a 1° latitude and 1° longitude grid. To define the MJO phase and amplitude, the  
145 Real-time Multivariate MJO (RMM, Wheeler and Hendon 2004) indices are calculated with the  
146 OLR and zonal winds at 850 and 200hPa. Predicted RMMs are obtained by projecting the  
147 predicted anomalies onto the observed combined EOF eigenvectors following Vitart (2017).  
148 RMM amplitude is defined as  $\sqrt{RMM1^2 + RMM2^2}$  (Wheeler and Hendon 2004). We evaluate  
149 MJO predictions during boreal winter (reforecasts initialized between October 1<sup>st</sup> and March  
150 31<sup>st</sup>). Climatology and anomalies are calculated over each day of the reforecast period, which  
151 ranges from 17 to 20 years among the models (Table 1). Given the long duration of the reforecast  
152 periods from each model, the composites and MJO skill presented in this study constitute a  
153 representative distribution of MJO events and differences in reforecast period and initialization  
154 interval among the models do not alter the overall conclusions.

155

### 156 **3. MJO Prediction and Propagation**

#### 157 *3.1 MJO prediction skill and biases*

158 We first compare the MJO prediction skill, mean amplitude bias and mean phase biases  
159 based on conventional skill metrics described in Kim et al. (2018). Figure 1a shows the RMM  
160 bivariate correlation coefficients (RMM skill, hereafter) as a function of forecast lead time  
161 during boreal winter for all MJO initial phases and amplitudes. The lead time when models reach

162 correlation coefficient 0.5 (an indicator of useful skill) is about 20~22-day in RSMAS-CCSM4,  
163 Navy-ESPC, and ESRL-FIM, and 25~27-day in KMA-GloSea5, NCEP-GEFS, NASA-GEOS5,  
164 NCAR-CESM1, and 33-day in ECMWF-CY43R3. Compared to the previous version (CY40R1)  
165 of the ECMWF system (Kim 2017), RMM skill is increased about 2-3 days in CY43R3. Overall,  
166 SubX models have skill comparable to S2S models (Vitart 2017; Lim et al. 2018; Janiga et al.  
167 2018; Pegion et al. 2019). As demonstrated in many studies, RMM skills are greater (lower) for  
168 forecasts with strong (weak) MJO events at initialization time (not shown). Generally, models  
169 with a relatively larger number of ensembles or with more frequent initialization (ECMWF-  
170 CY43R3, NCAR-CESM1, NASA-GEOS5) show higher skill, although the sensitivity of  
171 ensemble number and initialization frequency to the RMM skill needs to be examined in more  
172 detail.

173 Hereafter, only events with initially strong MJO (RMM amplitude >1.0) during winter are  
174 examined unless otherwise stated. The total number of selected strong MJO events in each  
175 reforecast are indicated in Figure 2. For example, for NCEP-GEFS, 270 events are selected  
176 based on the observed RMM amplitude and phase at day-0 of each forecast and compared with  
177 the observation as a function of forecast lead time. Figure 1b shows the mean amplitude bias  
178 relative to the observation for initially strong MJO cases. The mean amplitude bias is  $1/n \sum (F'_A - O'_A)$ ,  
179 where  $n$  is the number of selected events and subscript  $A$  denotes the RMM  
180 amplitude of ensemble mean forecast anomalies ( $F'$ ) and observed anomalies ( $O'$ ) as a function  
181 of forecast lead time. Consistent with S2S models (Vitart 2017; Lim et al. 2018; Wang et al.  
182 2018), most of the models tend to lose the amplitude as forecast time increases (Fig. 1b). Some  
183 models (NASA-GEOS5 and RSMAS-CCSM4) overestimate the amplitude during the first two  
184 weeks. Consistent with Janiga et al. (2018), Navy-ESPC produces stronger amplitudes than

185 observation after 10-days. To better understand the source of the bias, amplitude bias is  
186 compared by initial MJO phases (Fig. 2). During the first 10-days (gray vertical line), most  
187 models underestimate the amplitude when MJO locates initially over the Indo-Pacific warm pool  
188 (phase 1-4). NCAR-CESM1 and ECMWF-CY43R3 have overall weaker amplitude than the  
189 others. The reason for underestimation of MJO amplitude will be examined in later sections.

190 Figure 1c shows the mean phase bias for initially strong MJO cases. The mean phase bias is  
191 defined as  $1/n \sum (F_P' - O_P')$ , where subscript P denotes the phase defined as the phase angle (°)  
192 on the RMM phase-space diagram (details in Kim et al. 2018). Similar to S2S models (Vitart  
193 2017; Lim et al. 2018), all SubX models show negative values throughout the whole forecast  
194 period, indicating a slower propagation relative to the observation. When divided into initial  
195 MJO phases, this slower propagation appears in most of phases (not shown). The phase bias  
196 could be sensitive to MJO metrics. For example, the Navy-ESPC MJO was shown to be too fast  
197 in OLR (Janiga et al. 2018) while it is slow in the RMM measure.

### 198 *3.2 MJO propagation*

199 To further understand the predicted characteristics and biases associated with MJO eastward  
200 propagation over the Indo-Pacific, strong MJO events initialized at phase 1 and 2 are selected.  
201 Phase 1 and 2 are the phases in which the MJO convective signal is located over the central  
202 Indian Ocean and in which most models predict weaker and slower propagation through the MC  
203 than observed (Fig. 1 and 2). Although the spatial patterns of the MJO are slightly different  
204 between phase 1 and 2, we combine these two phases to increase the sample size. To avoid the  
205 double counting in observation due to sequential days that meets the criteria in a single strong  
206 MJO event, we screen the data with a 5-day interval which approximately matches with the  
207 initialization frequency in the reforecasts. In observations, a total of 246 initially strong MJO

208 phase 1 and 2 events are selected over 38 winters (1979-2017), while it ranges from 66 to 277 in  
209 models due to different initialization frequency and reforecast period. A 5-day moving average  
210 and 9-grid-point smoothing are applied for better visualization for Figure 3-5 and 7-8 (indicated  
211 in each figure). Day-01 composite, for example, is the average of forecast day 1 to 5, day-02 is  
212 average of day 2 to 6, and so on. Observed MJO propagation characteristics will be discussed  
213 first, followed by model comparison.

214 Figure 3 shows the composites of OLR and 850 hPa horizontal wind anomalies at forecast  
215 day-01. In observations (Fig. 3a), enhanced convection is centered over the equatorial Indian  
216 Ocean and suppressed convection extends over a broad region from the eastern Maritime  
217 Continent to the western Pacific (approximately from 110°E to 180°E). Strong equatorial  
218 easterly wind anomalies to the east of the convective envelope are associated with the Kelvin  
219 wave response to the convective heating, and the Rossby wave response enhances the easterlies  
220 and poleward flow to the west of the suppressed anomaly (e.g., Adames and Kim 2016). After 10  
221 days (Fig. 4a), the MJO convective envelope has moved to the MC with particularly strong  
222 convection between the MC and Australia. The MJO-associated circulation induces positive  
223 zonal advection of the seasonal mean moisture to the southern MC, thus helping the MJO to  
224 detour south of the MC (Kim et al. 2017). At day-20 (not shown), the observed MJO convective  
225 envelope propagates into the Pacific warm pool and the suppressed anomaly appears in the  
226 Indian Ocean which is roughly a mirror image of the day-01 pattern. To visualize the broad-scale  
227 observed MJO propagation, OLR and zonal wind at 850 hPa (U850) anomalies are averaged  
228 over 20°S-20°N and displayed as a function of longitude and forecast lead (Fig. 5a). The OLR  
229 anomaly weakens as it approaches the MC (west of 120°E) at about day-10 and re-amplifies as it  
230 slowly propagates through the Timor Sea (around 120°E), a narrow channel between the

231 southern part of Indonesia and Northern Australia. Then, the convective anomaly approaches the  
232 dateline at around day-20. After day-10, the suppressed convective anomaly appears in the  
233 western Indian Ocean and propagates eastward. The U850 shows continuous eastward  
234 propagation associated with the convective anomalies (Fig. 5a).

235 Overall, the SubX and S2S reforecasts capture the broad MJO propagation structure in the  
236 OLR and wind anomalies but with phase and amplitude biases (Fig. 3-5). At day-01 (Fig. 3),  
237 which is an average of the first five days, models have a comparable pattern with the  
238 observation. However, the predicted amplitude in OLR in some models (NCEP-CESM1 and  
239 ECMWF-CY43R3) is already weaker than the observed, while others (RSMAS-CCSM4 and  
240 NASA-GEOS5) overpredict the amplitude, loosely consistent with Figure 2. The initial biases  
241 could be attributed to different convective parameterization because OLR bias develops quickly.  
242 Initialization data and assimilation methods can also impact the model difference at day-01,  
243 although reasons behind diverse initial biases are beyond the scope of this study. At day-10,  
244 predicted OLR and U850 anomalies become more diverse between the models in both phase and  
245 amplitude (Fig. 4).

### 246 *3.3 MJO propagation skill*

247 Several earlier studies have examined the development of biases in MJO phase and  
248 amplitude in dynamical forecasting systems using the RMM index (such as Fig. 1b and c).  
249 However, because the RMM index is global, it is an indirect measure of the ability of a model to  
250 capture MJO propagation through the MC. Moreover, because the fractional contribution of  
251 upper-level zonal wind (U200) to the RMM is considerably higher than the contribution of OLR  
252 and U850 anomalies, the RMM skill and biases mainly reflects the predicted U200 (e.g., Straub  
253 2013), leading to an overly optimistic estimate of the ability of a model to predict OLR and U850

254 anomalies. The RMM skill, amplitude and phase biases shown in Figure 1 and 2, therefore, do  
255 not directly translate the biases emanating from the propagation of MJO convection and low-  
256 level circulation which are more closely linked to cumulus parameterizations.

257 To directly measure the MJO propagation ability in models, mean pattern correlation  
258 coefficient (*PCC*) and mean absolute amplitude (*AMP*) are calculated. Strong MJO events  
259 initialized at phase 1 and 2 are selected. *PCC* is a pattern correlation coefficient between  
260 individual observed and ensemble mean forecast anomalies calculated over the tropical Indo-  
261 Pacific (40°E-200°E and 20°S-20°N) and then averaged over all selected events in each model.  
262 *AMP* is the absolute amplitude of individual ensemble mean forecasted (or observed) anomalies  
263 averaged over the tropical Indo-Pacific (40°E-200°E and 20°S-20°N) and then averaged over all  
264 selected events in each model. To compare the change in skill as a function of exact lead time,  
265 the five-day moving average is not applied when calculating the *PCC* and *AMP* shown in Figure  
266 6.

267 At day-01, models generally capture the observed dipole pattern of the MJO envelope over  
268 the Indo-Pacific (Fig. 3), resulting in a high *PCC* in all variables (Fig. 6a-c). Then the *PCC*  
269 decreases in all three variables reaching 0.5 before 10 days in all models with a faster drop in  
270 *PCC<sub>OLR</sub>* than *PCC<sub>U850</sub>* or *PCC<sub>U200</sub>*. As mentioned earlier, the RMM skill (> 3 weeks, Fig. 1a)  
271 leads to overly optimistic estimate of model MJO prediction ability. The relationship between  
272 RMM skill score for phase 1 and 2 (similar to Fig. 1a) only loosely matches the *PCC* of OLR and  
273 850 and 200 hPa zonal winds. However, similar, to Fig. 1b, a continuous loss of amplitude  
274 (*AMP*) can be found in all models (Fig. 6d-f), except Navy-ESPC. In addition, we find little  
275 relationship between the magnitude of the *AMP* biases and the *PCC*. A particularly fast decrease  
276 in *AMP* is seen in NCAR-CESM1, ECMWF-CY43R3, NCEP-GEFS which generally produce

277 high RMM or *PCC* skill. The range of biases of  $AMP_{OLR}$  are larger compared to the biases in  
278 circulations fields at the beginning of forecasts ( $< 1$  week), indicating a quick development of  
279 convection biases. NCAR-CESM1, ECMWF-CY43R3, and NCEP-GEFS underestimate the  
280  $AMP_{OLR}$ , while the rest of models overestimate it at the beginning of forecasts (Fig. 6d).

281

## 282 **4. MJO Processes and Mean State**

### 283 *4.1 Moisture advection processes*

284 To understand the sources of the biases in the MJO forecasts it is crucial to understand the  
285 representation of the processes associated with the MJO propagation. As mentioned in the  
286 introduction, studies have shown that the advection of the mean moisture by the MJO anomalous  
287 circulation is the key process that increases moisture to the east and decreases moisture to the  
288 west of the envelope of enhanced moisture associated with the MJO, thus controlling the  
289 propagation (e.g., D. Kim et al. 2014; Adames and Kim 2016; Jiang et al. 2018). Therefore,  
290 GCMs with dry mean biases tend to have weaker moisture advection and worse MJO  
291 propagation (Gonzalez and Jiang 2017) and lower MJO prediction skill (Lim et al. 2018). Here,  
292 we test whether the relationship between MJO propagation process and mean moisture applies to  
293 the models from SubX and S2S. The seasonal mean moisture advection by the anomalous wind,  
294  $-V' \cdot \nabla \bar{Q}_{850}$ , is calculated where  $V'$  is the horizontal wind anomaly at 850 hPa and  $\bar{Q}_{850}$  is the  
295 winter climatology of specific humidity at 850 hPa, where the overbar denotes the climatology  
296 defined as the average of the first 4-weeks (1 to 28 forecast lead days). In order to smooth the  
297 horizontal moisture gradient ( $\nabla \bar{Q}_{850}$ ), especially the strong gradients in the vicinity of the MC

298 region due to land-ocean contrasts, we interpolate both  $\bar{Q}_{850}$  and  $V'$  from  $1.0^\circ$  to  $2.5^\circ$  in both  
 299 observations and reforecasts.

300 Studies have typically focused on moisture at 700 hPa (e.g., Gonzalez and Jiang 2017) but  
 301  $Q_{850}$  is the only common moisture variable available in the SubX reforecasts. One may argue  
 302 that 850 hPa level in the tropics is only marginally above the planetary boundary layer and  $Q_{850}$   
 303 may not represent the column moisture field. To justify the use of  $Q_{850}$  in representing the  
 304 column moisture, we compare the column-integrated  $Q$  ( $\langle Q \rangle$ ) and  $MSE$  ( $\langle MSE \rangle$ ) calculated by  
 305 ERAI over eight vertical levels from 1000 hPa to 100 hPa. Then, variables averaged over the  
 306 Indo-Pacific (Fig. 7, green box,  $80^\circ\text{E}$ - $130^\circ\text{E}$ ,  $20^\circ\text{S}$ - $15^\circ\text{N}$ ) are compared as a function of forecast  
 307 lead days when MJO starts from phase 1 and 2. The tendency and horizontal advection of  $Q_{850}$ ,  
 308  $\langle Q \rangle$ , and  $\langle MSE \rangle$  are similar to each other (not shown), although the overall pattern of  $Q_{850}$  is  
 309 noisier than the column-integrated variables.

310 Figure 7 shows the anomalous horizontal advection of winter mean specific humidity ( $-V' \cdot$   
 311  $\nabla \bar{Q}_{850}$ ) and anomalous wind at 850 hPa ( $V'$ ) at day-01 (day 1 to 5 average) in observations and  
 312 the reforecasts. In observations (Fig. 7a), the easterly and poleward wind to the east of the  
 313 convection anomaly and the winter mean moisture ( $\bar{Q}_{850}$ ) distribution (Fig. 9a) together induce  
 314 moisture advection on the poleward side of the MC consistent with previous studies (D. Kim et  
 315 al. 2014; Wang et al. 2017). The moisture recharge process is clearer if free tropospheric (such as  
 316 700 hPa) moisture observations are used but the overall behavior is similar (not shown). The  
 317 positive moisture advection over the MC at day-01 helps the MJO in the Indian Ocean to  
 318 propagate to the MC region after ten days as shown in Fig. 4a. To summarize the evolution of the  
 319 moisture advection,  $-V' \cdot \nabla \bar{Q}_{850}$  is averaged over a broad MC area (green box in Fig. 7). In  
 320 observations,  $-V' \cdot \nabla \bar{Q}_{850}$  is positive for up to two-weeks indicating a continuous moisture

321 advection to the MC area (Fig. 8a). This sustained moisture advection helps the MJO convective  
322 anomaly to propagate through the MC. After about two weeks, negative moisture advection  
323 helps the suppressed MJO phase to propagate over the MC. The moisture advection from  $-V' \cdot$   
324  $\nabla \bar{Q}_{850}$  is approximately in phase with the moisture tendency and dominant among other terms  
325 and  $90^\circ$  out of phase with the moisture and OLR anomaly (not shown) as discussed in previous  
326 studies (e.g., D. Kim et al. 2014; Jiang 2017).

327 Models generally capture the pattern of the  $-V' \cdot \nabla \bar{Q}_{850}$  at day-01 (Fig. 7b-i). However, the  
328 amplitude of moisture advection declines rapidly in all models (Fig. 8a), which gives rise to a  
329 weaker amplitude of moisture advection than the observed during the entire forecast period.  
330 During the first 10-days (Fig. 8b), the multi-model mean (MMM) of moisture advection is only  
331 61.7 % of the observed value, and individual model ranges from 41.1 % (ESRL-FIM) to 80.0 %  
332 (NASA-GEOS5). It can be concluded that all SubX and S2S models predict weaker moisture  
333 advection than is seen in observations. This is consistent with the underprediction of MJO  
334 amplitude in most of the models (Fig. 6). The underprediction of MJO amplitude, however,  
335 could be associated with other MJO intensification processes as well, such as surface-fluxes  
336 (e.g., Sobel et al. 2010) or radiative-convective feedbacks (e.g., Raymond 2001). In addition,  
337 these processes could explain why the Navy-ESPC system overpredicts the amplitude of the  
338 MJO. Navy-ESPC has a negative OLR mean state bias over the active MJO region (not shown)  
339 which suggests it may be overestimating the strength of radiative-convective feedbacks.

#### 340 *4.2 Mean moisture biases*

341 Two variables can impact the horizontal moisture advection ( $-V' \cdot \nabla \bar{Q}_{850}$ ): wind anomalies  
342 ( $V'$ ) and the mean moisture distribution ( $\nabla \bar{Q}_{850}$ ). In the previous version of the ECMWF system,  
343 the quickly developing mean moisture bias has larger contributions to the moisture advection

344 bias than the MJO wind anomalies (Kim 2017). Observed  $\bar{Q}_{850}$  and model biases of  $\bar{Q}_{850}$  are  
345 compared in Figure 9 with land areas masked out due to the influence of terrain. During boreal  
346 winter, observed  $\bar{Q}_{850}$  is maximized in the tropical eastern MC, inducing both strong zonal and  
347 meridional gradient of  $\bar{Q}_{850}$ , while all reforecasts show dry biases over the tropical Indo-Pacific  
348 region (Fig. 9). RSMAS-CCSM4, NCEP-GEFS, KMA-GloSea5 have an approximately 5%  
349 reduction of  $\bar{Q}_{850}$  in the tropical Indo-Pacific (40°E-200°E, 15°S-15°N) relative to observations,  
350 while Navy-ESPC, ESRL-FIM, and NASA-GEOS5 have an approximately 10% reduction. Dry  
351 biases are relatively small (<1 %) in NCAR-CESM1 and ECMWF-CY43R3.

352 The meridional moisture advection has a larger contribution to MJO propagation than the  
353 zonal component in both observation and reforecasts (D. Kim et al. 2014; Kim 2017; Lim et al.  
354 2018). The meridional gradient of  $\bar{Q}_{850}$  (hereafter  $\bar{Q}_y$ ) is defined by simply taking the difference  
355 between the equatorial (80°E-130°E, 10°S-5°N) and average of two subtropical regions (80°E-  
356 130°E, 5°N-15°N and 80°E-130°E, 20°S-10°S), similar to Lim et al. (2018). Because of the  
357 decrease of moisture in poleward direction, observation shows strong negative meridional  
358 gradient ( $\bar{Q}_y = -1.7$  g/kg) while all models predict weaker meridional gradient ranging from -1.3  
359 (ECMWF-CY43R3) to positive values of 1.0 g/kg (NASA-GEOS5). Simulation of positive  $\bar{Q}_y$   
360 (poleward increase of mean moisture) in NASA-GEOS5 and ESRL-FIM is due to weak moisture  
361 in the MC area where the observation has a maximum. Basin-wide dry bias and weaker  
362 meridional moisture gradient can partially contribute to weaker horizontal moisture advection  
363 shown in Fig. 8.

364 Kim (2017) and Lim et al. (2018) argued that models with larger mean moisture pattern  
365 biases have weaker moisture advection, fast damping of MJO propagation, and thus lower MJO  
366 prediction skill. However, among the models examined here, we do not find significant linear

367 relationships between the mean moisture pattern, moisture advection, propagation and prediction  
368 skills. For example, NASA-GEOS5 shows the largest biases in  $\bar{Q}_{850}$  and  $\bar{Q}_y$  (Fig. 9h) but has the  
369 strongest moisture advection ( $-V' \cdot \nabla \bar{Q}_{850}$ ) among models (Fig. 8). On the other hand, ECMWF  
370 has the smallest mean state bias but shows fast damping of the moisture advection, but high  
371 prediction skill. This is because moisture advection ( $-V' \cdot \nabla \bar{Q}_{850}$ ) could also be attributed to the  
372 MJO circulation anomalies ( $V'$ ). Weaker moisture advection shown in ECMWF-CY43R3 could  
373 result from the weaker wind anomalies, although the mean state bias is simulated reasonably.  
374 Stronger moisture advection in NASA-GEOS5 could result from the stronger wind, although the  
375 mean state bias is worse. Both models, however, have high RMM skills (Fig. 1a). Therefore,  
376 from eight models, it is hard to link the mean state bias directly to moisture advection  
377 performance, propagation and prediction skill. Biases in MJO associated fields (e.g. convection)  
378 and mean state cannot be clearly separated due to their interaction and tight coupling between  
379 each other. Further research with sensitivity experiments is needed. Nonetheless, it is clear that  
380 all SubX and S2S models examined in this study have dry biases in low-tropospheric moisture  
381 and simulate weaker moisture advection than observation which could potentially impact MJO  
382 propagation and limit the prediction skill.

#### 383 *4.3 Precipitation-moisture coupling and precipitation biases*

384 To further understand the sources of the low-tropospheric dry biases shown in the SubX and  
385 S2S models, the simulation of precipitation-moisture coupling is evaluated. Tropical moisture is  
386 strongly coupled to precipitation and convection processes (e.g., Holloway and Neelin 2009) and  
387 the representation of these processes are sensitive to convective parameterization in numerical  
388 models. In the GPCP observations (Fig. 10a), the maximum winter mean precipitation is along  
389 the Intertropical Convergence Zone (ITCZ), South Pacific Convergence Zone (SPCZ) and over

390 the MC. Figure 10 shows that models over predict precipitation over the western Indian Ocean as  
391 well as western Pacific with a well-known double ITCZ biases (Lin 2007). In summary, models  
392 tend to predict excess surface precipitation and have a lower-tropospheric dry bias over the Indo-  
393 Pacific region. These mean biases develop quickly and saturate in the first week.

394 To further understand the source of precipitation biases, the occurrence frequency (%) of  
395 daily total precipitation rates are compared (Fig. 11a). To calculate the occurrence frequency,  
396 first the number of occurrences in each precipitation rate bin is divided by the total number of  
397 days for each forecast lead time. Then the average across the first 4 weeks over the Indo-Pacific  
398 Ocean (60°E-180°E, 15°S-15°N) is computed from this; land area is masked out since convection  
399 is typically forced by the diurnal cycle more than moisture-convection coupling (Ahmed and  
400 Schumacher 2017). Only control simulations are used from the reforecasts in these calculations.  
401 Precipitation rates are binned with logarithmic bin sizes to account for more frequent events at  
402 low precipitation rates (Fig. 11a). Precipitation rates less than 0.01 mm/day are cut off. GPCP  
403 observations have a broad maximum in occurrence between 10 to 20 mm/day consistent with  
404 TRMM precipitation estimates (Kim et al. 2015). NCEP-GEFS has uneven distribution for  
405 precipitation rates at < 10 mm/day, and such distributions is seen in other areas, while the reason  
406 is not clear at this stage. All models produce frequent precipitation in light regimes (< 10  
407 mm/day) and most of them underestimate the heavy precipitation regime (> 20 mm/day), except  
408 ESRL-FIM, NCEP-GEFS, and Navy-ESPC which overestimate frequency for > 40 mm/day. The  
409 most frequent precipitation rate is 15 mm/day in observations, 10 mm/day in NCAR-CESM1,  
410 ECMWF-CY43R3, and KMA-GloSea5, 5 mm/day in RSMAS-CCSM4 and NASA-GEOS5 and  
411 2 mm/day in ESRL-FIM and Navy-ESPC. NCAR-CESM1, ECMWF-CY43R3, and KMA-  
412 GloSea5 have almost twice as frequent precipitation as that observed around 10 mm/day.

413 Overall, SubX and S2S reforecasts produce light precipitation that is too frequent which may be  
414 associated with the dry biases in the low-tropospheric mean state (Fig. 9).

415 Previous studies have shown the importance of low-tropospheric moisture to the onset of  
416 deep convection in the tropics (e.g., Bretherton et al. 2004; Peters and Neelin 2006; Holloway  
417 and Neelin 2009; Rushley et al. 2018). Over tropical oceans, a sharp increase in precipitation rate  
418 occurs when column relative humidity reaches about 80 % saturation and continues to increase  
419 exponentially at higher saturations. However, this precipitation pickup tends to occur earlier than  
420 observed in most GCMs which causes these models to overestimate precipitation in dry regimes  
421 and underestimate it in humid regimes (Rushley et al. 2018). This common moisture-  
422 precipitation coupling bias can directly influence the simulation of MJO propagation (Kim et al.  
423 2012; Jiang et al. 2015; Ahn et al. 2017). To evaluate the predicted moisture-precipitation  
424 coupling in the SubX and S2S reforecasts, daily total precipitation and  $Q_{850}$  are compared. Note  
425 that  $Q_{850}$  is the daily mean specific humidity field from observation and control simulations, not  
426 the climatology ( $\bar{Q}_{850}$ ). Figure 11b shows the mean distribution of precipitation rate in each  $Q_{850}$   
427 bin averaged over the first 4-weeks over the tropical Indo-Pacific (60°E-180°E, 15°S-15°N) with  
428 land areas masked out. These results are not sensitive to the choice of the forecast lead since the  
429 biases develop in the first week of the forecasts. In observations, precipitation pickup begins  
430 around 10.5 g/kg, increases slowly up to about 12 g/kg, and increases exponentially beyond that  
431 (Fig. 11b). The inset in Figure 11b provides a closeup of the precipitation rates during drier  
432 conditions and shows the earlier onset of deep convection in all models compared to the  
433 observation. Recall from Figure 11a that these light precipitation rates are not rare and in fact  
434 occur more frequently in models than in observations. In summary, models overall predict larger

435 mean precipitation rates and more frequent precipitation in the lower humidity regime than in  
436 observations.

437

## 438 **5. Summary and Discussion**

439 In this study, MJO prediction skill, propagation processes, mean state biases, and  
440 precipitation-moisture coupling are evaluated in reforecasts from models in the SubX and S2S  
441 databases. Overall, SubX models show comparable RMM skill ranges (3-4 weeks) to S2S  
442 models and capture the broad structure of the MJO convective envelope at the beginning of the  
443 forecast. However, SubX and S2S models fail to predict the propagation of the MJO convection  
444 beyond 10-days with most of them having a fast decay in the amplitude of the convection  
445 associated with the MJO. To better understand the biases associated with the MJO propagation,  
446 we evaluate each model's capability to represent moisture advection processes and relate this to  
447 mean moisture biases through the framework of the moisture mode theories (e.g., Raymond and  
448 Fuchs 2009; Sobel and Maloney 2012, 2013). Compared to observations, the horizontal moisture  
449 advection east of the MJO convective anomaly is underestimated in all models, primarily due to  
450 the underestimation of the meridional component of the horizontal moisture advection. This  
451 weak horizontal moisture advection is partly associated with dry biases in the lower-tropospheric  
452 across the Indo-Pacific.

453 Lim et al. (2018) demonstrated that MJO prediction skill and the bias pattern of the mean  
454 column-integrated water vapor are significantly correlated in seven S2S models. In this study, we  
455 do not find a strong correlation between biases in the horizontal moisture advection  
456 representation or mean moisture pattern with MJO prediction skill. This discrepancy could be  
457 due to our focus on moisture at 850 hPa, whereas Lim et al. (2018) used column-integrated

458 moisture. On the other hand, it could indicate that we do not yet fully understand all the different  
459 pathways in which biases in MJO propagation can arise due to errors in the representation of  
460 physical processes. For example, while our focus is mainly on horizontal moisture advection  
461 process, recent studies have shown that the vertical moisture advection also plays an important  
462 role in MJO propagation (Janiga and Zhang 2016; Wang et al. 2017). MJO propagation biases  
463 can also emanate from other processes such as the longwave cloud-radiation feedback (Lim et al.  
464 2018), air-sea coupling (e.g., Demott et al. 2016), and diurnal cycle in the MC region (Zhang and  
465 Ling 2017). A more complete understanding of the contribution of these processes to errors in  
466 MJO propagation would lead to further improvements in MJO prediction skill.

467       SubX and S2S reforecasts contain the following biases over the tropical Indo-Pacific: a dry  
468 lower troposphere, excess of surface precipitation, more frequent occurrence of light  
469 precipitation rates, and a transition to stronger precipitation rates that begins at lower humidity  
470 than is seen in observations. This indicates that convection occurs too frequently in models and is  
471 not sufficiently inhibited when tropospheric moisture is low, which is likely due to the  
472 representation of entrainment. Previous studies have shown that changes in the representation of  
473 entrainment through increasing the sensitivity of deep convection to the environmental humidity  
474 generally improves MJO simulation (Tokioka et al. 1988; Bechtold et al. 2008, Hannah and  
475 Maloney 2011; Kim et al. 2012; Hirons et al. 2013, Klingaman and Woolnough 2014; Jiang et al.  
476 2015) while degrading the mean state (Kim et al. 2011). Through increased entrainment rate,  
477 more moisture is likely to build up and precondition the deep convection while suppressing  
478 premature development of convection, thus improving MJO simulation (e.g., review by Kim and  
479 Maloney 2017). In other words, with low entrainment rate in the deep convective scheme,  
480 convection occurs before the lower troposphere is sufficiently moistened (i.e., insufficient

481 conditional instability) (Kuo et al. 2017). This results in a moisture-depleted atmosphere because  
482 atmospheric moisture can be removed efficiently through convection-induced precipitation thus  
483 the environment favors a low humidity state (Kuo et al. 2017). Given that the SubX and S2S  
484 models have precipitation occurring in the lower humidity regime and possess climatological dry  
485 biases in the lower-troposphere, it is likely that those models have lower sensitivity of the  
486 convection to environmental moisture which can be related to the entrainment rate. However,  
487 with the limited output variables and lack of detailed information about each model's convection  
488 scheme, discussing the impact of model parameterization to MJO prediction is beyond the scope  
489 of this study. Additional output of model variables would help to resolve these issues.

490

491

492 **Acknowledgments**

493 HK was supported by NSF grant AGS-1652289, NOAA grant NA16OAR4310070, and the  
494 KMA R&D Program grant KMI2018-03110. GloSea5 reforecast was provided by Dr. Myong-In  
495 Lee from UNIST. MJ and the generation of the Navy-ESPC forecasts were supported by the  
496 Office of Naval Research and N2N6E through the Navy Earth System Prediction Capability  
497 Effort, and the Chief of Naval Research through the NRL Base Program (PE 0601153N). Navy-  
498 ESPC forecasts were performed as part of the NMME-SubX experiment funded by the NOAA-  
499 Modeling, Analysis, Predictions, and Projections (MAPP) Program (NOAA-OAR-CPO-2016-  
500 2004413). Computational resources were supported in part by a grant of time from the High  
501 Performance Computing Modernization Program and the Navy-ESPC forecasts were integrated  
502 at the Navy Department of Defense Supercomputing Resource Center, Stennis Space Center,  
503 Mississippi. The sources of data used in this study are: <http://cola.gmu.edu/kpegion/subx/> for  
504 SubX reforecasts, <http://s2sprediction.net/> S2S reforecasts,  
505 <http://apps.ecmwf.int/datasets/data/interim-full-daily> for ERA-Interim.

506

507

508 **References**

- 509 Adames, A. F. and D. Kim (2016), The MJO as a convectively coupled moisture wave: theory  
510 and observations, *J. Atmos. Sci.*, 73, 913–941.
- 511 Ahn, M. S., and coauthors (2017), MJO simulation in CMIP5 climate models: MJO skill metrics  
512 and process-oriented diagnosis, *Clim. Dyn.* doi:10.1007/s00382-017-3558-4.
- 513 Bechtold, P., M. Köhler, T. Jung, F. Doblas-Reyes, M. Leutbecher, M. J. Rodwell, F. Vitart, and  
514 G. Balsamo (2008), Advances in simulating atmospheric variability with the ECMWF  
515 model: From synoptic to decadal time-scales. *Quart. J. Roy. Meteor. Soc.*, 134, 1337–1351,  
516 doi:10.1002/qj.289
- 517 Bretherton, C. S., M. E. Peters, and L. E. Back (2004), Relationships between water vapor path  
518 and precipitation over the tropical oceans. *J. Climate*, 17, 1517-1528.
- 519 Dee, D. P., and coauthors (2011), The ERA-Interim reanalysis: configuration and performance of  
520 the data assimilation system. *Q. J. R. Meteorol. Soc.*, 137, 553-597.
- 521 DeMott, C. A., N. P. Klingaman, and S. J. Woolnoug (2015), Atmosphere-ocean coupled  
522 processes in the Madden-Julian oscillation, *Rev. Geophys.*, 53, doi:10.1002/2014RG000478.
- 523 Gonzalez, A. and X. Jiang (2017), Winter Mean Lower-Tropospheric Moisture over the  
524 Maritime Continent as a Climate Model Diagnostic Metric for the Propagation of the  
525 Madden-Julian Oscillation. *Geophys. Res. Lett.*, 44, doi:10.1002/2016GL072430.
- 526 Hannah, W. M. and E. D. Maloney (2011), The Role of Moisture–Convection Feedbacks in  
527 Simulating the Madden–Julian Oscillation. *J. Climate*, 24, 2754–2770,  
528 <https://doi.org/10.1175/2011JCLI3803.1>

- 529 Hannah, W. M., and E. D. Maloney (2014), The moist static energy budget in NCAR CAM5  
530 hindcasts during DYNAMO, *J. Adv. Model. Earth Syst.*, 6, 420–440.
- 531 Hannah, W. M., E. D. Maloney, and M. S. Pritchard (2015), Consequences of Systematic Model  
532 Drift in DYNAMO Hindcasts with SP-CAM and CAM5, *J. Adv. Model. Earth Syst.*, 7.
- 533 Hirons, L. C., Inness, P., Vitart, F. and Bechtold, P (2013), Understanding advances in the  
534 simulation of intraseasonal variability in the ECMWF model. Part I: the representation of  
535 the MJO. *Q. J. R. Meteorol. Soc.*, 139 (675). pp. 1417-1426. ISSN 1477-870X doi:  
536 10.1002/qj.2060
- 537 Holloway, C. E., and J. D. Neelin (2009), Moisture vertical structure, column water vapor, and  
538 tropical deep convection. *J. Atmos. Sci.*, 66, 1665–1683,  
539 <https://doi.org/10.1175/2008JAS2806.1>.
- 540 Huffman, G. J., R. F. Adler, M. M. Morrissey, D. T. Bolvin, S. Curtis, R. Joyce, B. McGavock,  
541 and J. Susskind (2001), Global Precipitation at One-Degree Daily Resolution from  
542 Multisatellite Observations. *J. Hydrometeor.*, 2, 36–50
- 543 Janiga, M. A. and C. Zhang (2016), MJO Moisture Budget during DYNAMO in a Cloud-  
544 Resolving Model. *J. Atmos. Sci.*, 73, 2257–2278, <https://doi.org/10.1175/JAS-D-14-0379.1>
- 545 Janiga, M. A., C. J. Schreck, J. A. Ridout, M. Flatau, N. P. Barton, E. J. Metzger, and C. A.  
546 Reynolds (2018), Subseasonal Forecasts of Convectively Coupled Equatorial Waves and the  
547 MJO: Activity and Predictive Skill. *Mon. Wea. Rev.*, 146, 2337–2360,  
548 <https://doi.org/10.1175/MWR-D-17-0261.1>
- 549

- 550 Jiang X. (2017), Key processes for the eastward propagation of the Madden-Julian Oscillation  
551 based on multi-model simulations. *J. Geophys. Res. Atmos.*, 122,  
552 doi:10.1002/2016JD025955.
- 553 Jiang, X., D. E. and coauthors (2015), Vertical structure and diabatic processes of the Madden-  
554 Julian Oscillation: Exploring Key Model Physics in Climate Simulations, *J. Geophys. Res.*  
555 *Atmos.*, 120, 4718-4748.
- 556 Jiang, X., A. F. Adames, M. Zhao, D. E. Waliser, and E. D. Maloney (2018), A Unified Moisture  
557 Moist Framework for Seasonality of MJO Propagation. *J. Climate*,  
558 <https://doi.org/10.1175/JCLI-D-17-0671.1>
- 559 Kim, D., A. H. Sobel, E. D. Maloney, D. M. W. Frierson, I. S. Kang (2011), A systematic  
560 relationship between intraseasonal variability and mean state bias in AGCM simulations, *J.*  
561 *Climate*, 24 (21), 5506-5520.
- 562 Kim, D., A.H. Sobel, A.D. Del Genio, Y. Chen, S.J. Camargo, M. Yao, M. Kelley, and L.  
563 Nazarenko (2012), The Tropical Subseasonal Variability Simulated in the NASA GISS  
564 General Circulation Model. *J. Climate*, 25, 4641–4659, [https://doi.org/10.1175/JCLI-D-11-](https://doi.org/10.1175/JCLI-D-11-00447.1)  
565 00447.1
- 566 Kim, D., M. Ahn, I. Kang, and A.D. Del Genio (2015), Role of Longwave Cloud–Radiation  
567 Feedback in the Simulation of the Madden–Julian Oscillation. *J. Climate*, 28, 6979–6994,  
568 <https://doi.org/10.1175/JCLI-D-14-00767.1>
- 569 Kim, D, H. Kim, and M.-I. Lee (2017), Why does the MJO detour the Maritime Continent  
570 during austral summer? *Geophys. Res. Lett.*, 44, 2579–2587,  
571 <https://doi.org/10.1002/2017GL072643>.

- 572 Kim, D., and E. D. Maloney (2017), Review: Simulation of the Madden-Julian oscillation using  
573 general circulation models. *The Global Monsoon System*, 3rd Edition, C.-P. Chang et al.,  
574 Eds.
- 575 Kim, D. and E. D. Maloney, and C. Zhang (2019), Review: MJO propagation over the Maritime  
576 Continent, *The Global Monsoon System*, C.-P. Chang et al., Eds., (accepted)
- 577 Kim, H. M. (2017), The impact of the mean moisture bias on the key physics of MJO  
578 propagation in the ECMWF reforecast, *J. Geophys. Res. Atmos.*, 122, 7772–7784.
- 579 Kim, H. M., P. J. Webster, V. E. Toma, and D. Kim (2014), Predictability and prediction skill of  
580 the MJO in two operational forecasting systems, *J. Climate*, 27 (14), 5364-5378.
- 581 Kim, H., F. Vitart, and D. E. Waliser (2018), Prediction of the Madden–Julian Oscillation: A  
582 Review. *J. Climate*, 31, 9425–9443
- 583 Kirtman, B. P. and coauthors (2017), The Subseasonal Experiment (SubX) [Data set]. IRI Data  
584 Library. <https://doi.org/10.7916/D8PG249H>
- 585 Klingaman, N. P., and coauthors (2015), Vertical structure and physical processes of the  
586 Madden–Julian Oscillation: Linking hindcast fidelity to simulated diabatic heating and  
587 moistening, *J. Geophys. Res. Atmos.*, 10.1002/2014JD022374.
- 588 Klingaman, N. P. and S. J. Woolnough (2014), Using a case-study approach to improve the  
589 Madden–Julian oscillation in the Hadley Centre model. *Q. J. R. Meteorol. Soc.*, 140: 2491-  
590 2505. doi:10.1002/qj.2314
- 591 Kuo, Y., J. D. Neelin, and C. R. Mechoso (2017), Tropical Convective Transition Statistics and  
592 Causality in the Water Vapor–Precipitation Relation. *J. Atmos. Sci.*, 74, 915–931,  
593 <https://doi.org/10.1175/JAS-D-16-0182.1>

- 594 Liebmann, B. and C. A. Smith (1996), Description of a Complete (Interpolated) Outgoing  
595 Longwave Radiation Dataset. *Bulletin of the American Meteorological Society*, 77, 1275-  
596 1277.
- 597 Lim, Y., S. Son, and D. Kim (2018), MJO prediction skill of the subseasonal-to-seasonal  
598 prediction models. *J. Climate*, <https://doi.org/10.1175/JCLI-D-17-0545.1>
- 599 Lin, J. (2007), The Double-ITCZ Problem in IPCC AR4 Coupled GCMs: Ocean–Atmosphere  
600 Feedback Analysis. *J. Climate*, 20, 4497–4525, <https://doi.org/10.1175/JCLI4272.1>
- 601 Ling J., P. Bauer, P. Bechtold, A. Beljaars, R. Forbes, F. Vitart, M. Ulate, and C. Zhang, (2014),  
602 Global versus Local MJO Forecast Skill of the ECMWF Model during DYNAMO. *Mon.*  
603 *Wea. Rev.*, 142, 2228-2247.
- 604 Liu, X., and coauthors (2017), MJO prediction using the sub-seasonal to seasonal forecast model  
605 of Beijing Climate Center. *Clim. Dyn.*, 48, 3283-3307.
- 606 Madden, R. A., and P. R. Julian (1971), Detection of a 40–50 day oscillation in the zonal wind in  
607 the tropical Pacific, *J. Atmos. Sci.*, 28, 702–708.
- 608 Madden, R. A., and P. R. Julian, (1972), Description of global-scale circulation cells in the  
609 tropics with a 40–50 day period, *J. Atmos. Sci.*, 29, 1109–1123.
- 610 Neena, J. M., J. Y. Lee, D. Waliser, B. Wang, X. Jiang, (2014), Predictability of the Madden–  
611 Julian Oscillation in the Intraseasonal Variability Hindcast Experiment (ISVHE). *J. Climate*,  
612 27, 4531-4543.
- 613 Pegion, K. and coauthors, (2019), The Subseasonal Experiment (SubX): A multi-model  
614 subseasonal prediction experiment, *BAMS* (submitted).

- 615 Peters, O. and J. D. Neelin (2006), Critical phenomena in atmospheric precipitation. *Nat. Phys.* 2,  
616 393–396.
- 617 Raymond, D.J., (2001), A New Model of the Madden–Julian Oscillation. *J. Atmos. Sci.*, 58,  
618 2807–2819.
- 619 Raymond, D.J. and Ž. Fuchs, (2009), Moisture Modes and the Madden–Julian Oscillation. *J.*  
620 *Climate*, 22, 3031–3046, doi: 10.1175/2008JCLI2739.1.
- 621 Rushley, S.S., D. Kim, and Á.F. Adames, (2019), Changes in the MJO under Greenhouse Gas–  
622 Induced Warming in CMIP5 Models. *J. Climate*, 32, 803–821, [https://doi.org/10.1175/JCLI-](https://doi.org/10.1175/JCLI-D-18-0437.1)  
623 [D-18-0437.1](https://doi.org/10.1175/JCLI-D-18-0437.1)
- 624 Sobel, A., and E. Maloney, (2012), An Idealized Semi-Empirical Framework for Modeling the  
625 Madden–Julian Oscillation. *J. Atmos. Sci.*, 69, 1691–1705.
- 626 ———, and ———, (2013), Moisture Modes and the Eastward Propagation of the MJO. *J. Atmos.*  
627 *Sci.*, 70, 187–192, doi:10.1175/JAS-D-12-0189.1.
- 628 Sobel, A. H., Maloney, E. D., Bellon, G., and Frierson, D. M., (2010), Surface Fluxes and  
629 Tropical Intraseasonal Variability: a Reassessment, *J. Adv. Model. Earth Syst.*, 2, 2,  
630 doi:10.3894/JAMES.2010.2.2.
- 631 Straub, K. H., (2013), MJO initiation in the real-time multivariate MJO index. *J. Climate*, 26,  
632 1130–1151, doi:10.1175/JCLI-D-12-00074.1
- 633 Tokioka, T., K. Yamazaki, A. Kitoh, and T. Ose, (1988), The equatorial 30–60 day oscillation  
634 and the Arakawa Schubert penetrative cumulus parameterization. *J. Meteor. Soc. Japan*, 66,  
635 883–901.

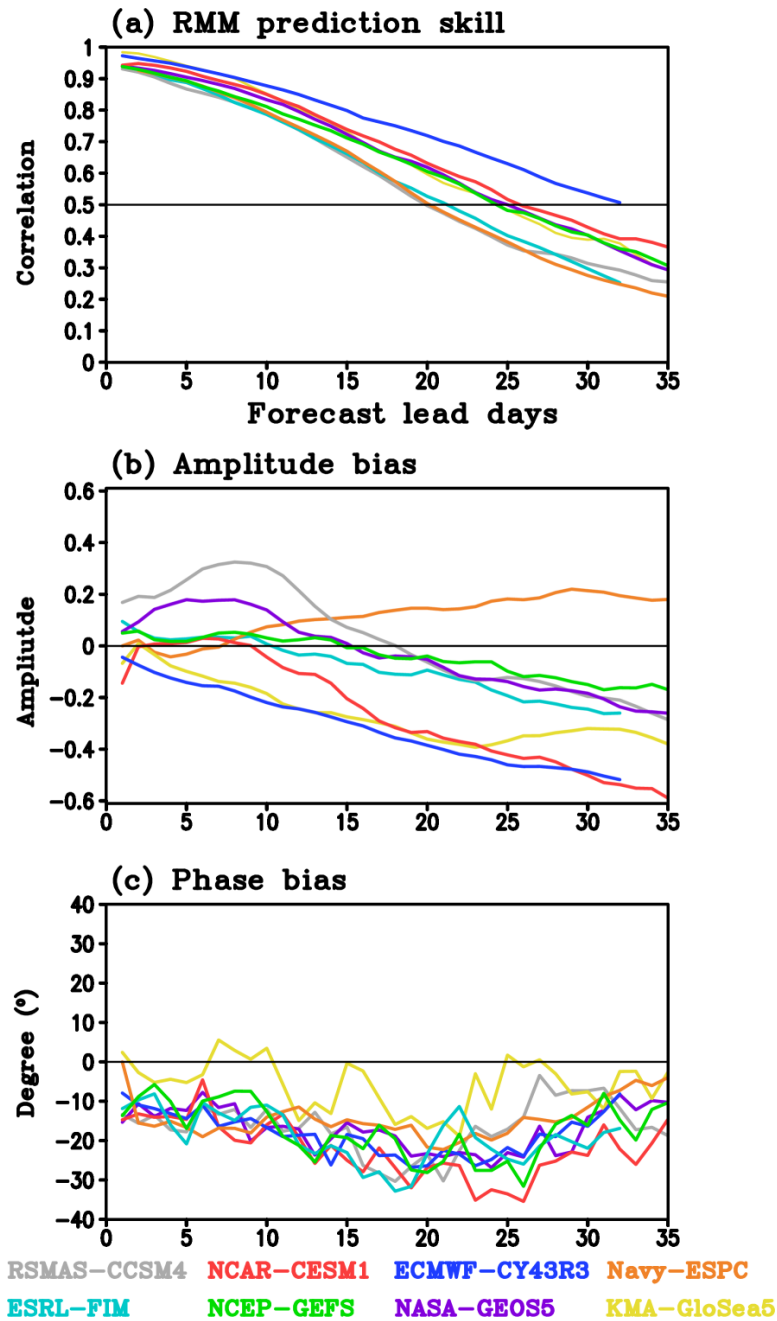
- 636 Vitart, F., (2017), Madden—Julian Oscillation prediction and teleconnections in the S2S  
637 database. *Q. J. R. Meteorol. Soc.*, 143: 2210–2220. doi:10.1002/qj.3079
- 638 Vitart, F. and coauthors, (2017), The Sub-seasonal to Seasonal Prediction (S2S) Project Database.  
639 *Bull. Amer. Meteor. Soc.*, doi: 10.1175/BAMS-D-16-0017.1.
- 640 Wang, L., T. Li, E. Maloney, and B. Wang, (2017), Fundamental Causes of Propagating and  
641 Nonpropagating MJOs in MJOTF/GASS models. *J. Climate*, 30, 3743-3769
- 642 Wang, S., A. H. Sobel, M. K. Tippett, F. Vitart. (2018), Prediction and predictability of tropical  
643 intraseasonal convection: seasonal dependence and the Maritime Continent prediction  
644 barrier. *Climate Dynamics*, doi.org/10.1007/s00382-018-4492-9
- 645 Wang, W., M. P. Hung, S. J. Weaver, A. Kumar, X. Fu, (2014), MJO prediction in the NCEP  
646 Climate Forecast System version 2, *Clim. Dyn.*, 10.1007/s00382-013-1806-9
- 647 Wheeler, M. C. and H. H. Hendon, (2004), An all-season real-time multivariate MJO index:  
648 Development of an index for monitoring and prediction, *Mon. Wea. Rev.*, 132, 1917–1932.
- 649 Zhang, C. and J. Ling, (2017), Barrier Effect of the Indo-Pacific Maritime Continent on the MJO:  
650 Perspectives from Tracking MJO Precipitation. *J. Climate*, 30, 10.1175/JCLI-D-16-0614.1,  
651 3439-3459.
- 652

653 Table 1. Hindcasts data information.

Model	Ensemble members	Initialization interval	Hindcast period	Source and References
NCEP-GEFS	11	1/week	1999-2015	SubX, Pegion et al. (2019)
NASA-GEOS5	4	every 5 days		
Navy-ESPC	4	1/week		
RSMAS-CCSM4	3	1/week		
ESRL-FIM	4	1/week		
NCAR-CESM1	20	1/week		
ECMWF-CY43R3	11	2/week	1997-2016	S2S, Vitart et al. (2017)
KMA/UKMO-GloSea5	3	4/month	1991-2010	

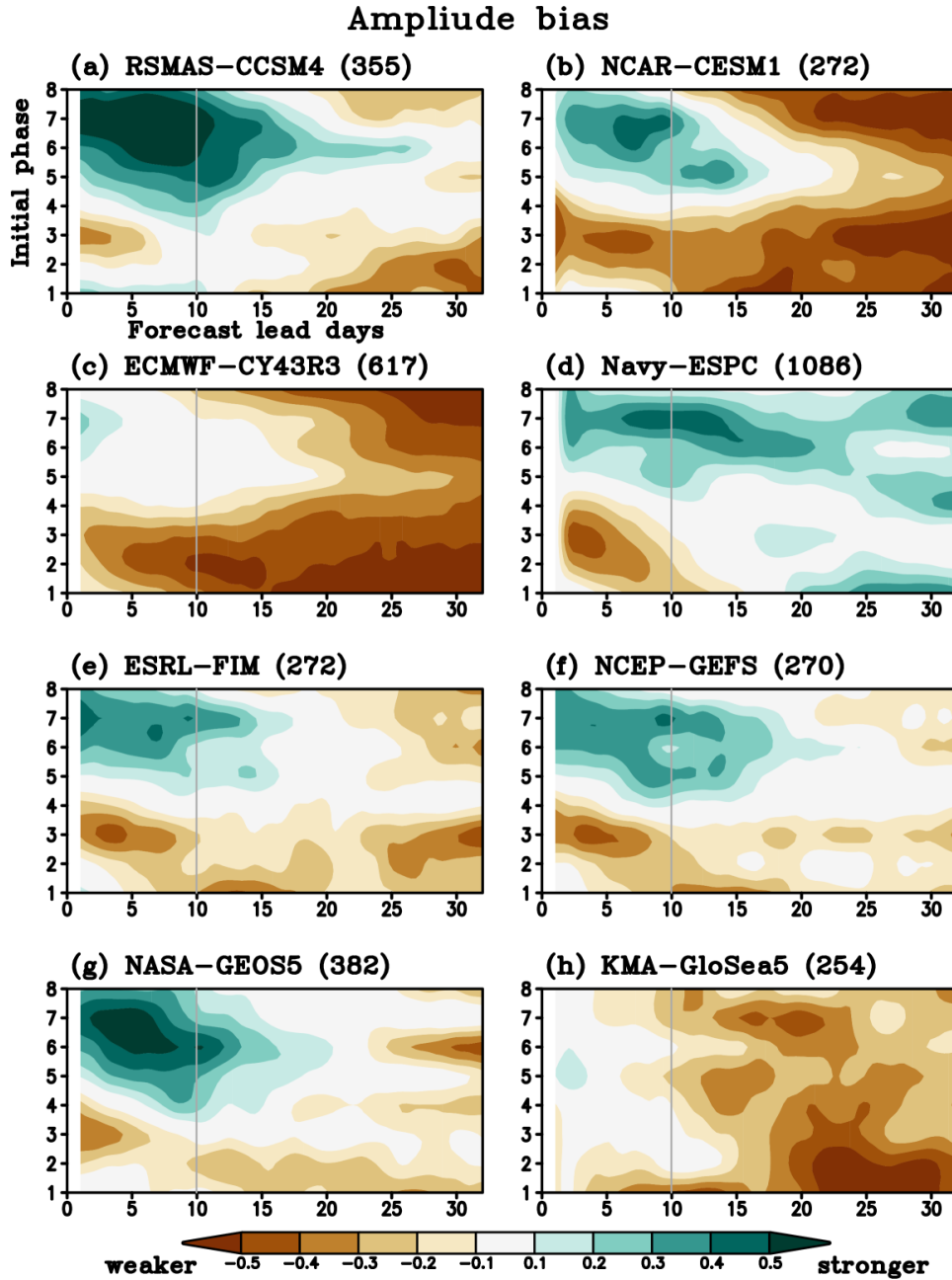
654

655



656

657 Figure 1: (a) RMM prediction skill (bivariate correlation coefficient) between the model  
 658 ensemble means and observation. Horizontal line denotes correlation of 0.5. (b)  
 659 Amplitude bias and (c) phase bias (°) relative to observation for initially strong MJOs.  
 660 Negative value in (b) and (c) indicates weaker and slower MJO than in observations,  
 661 respectively.



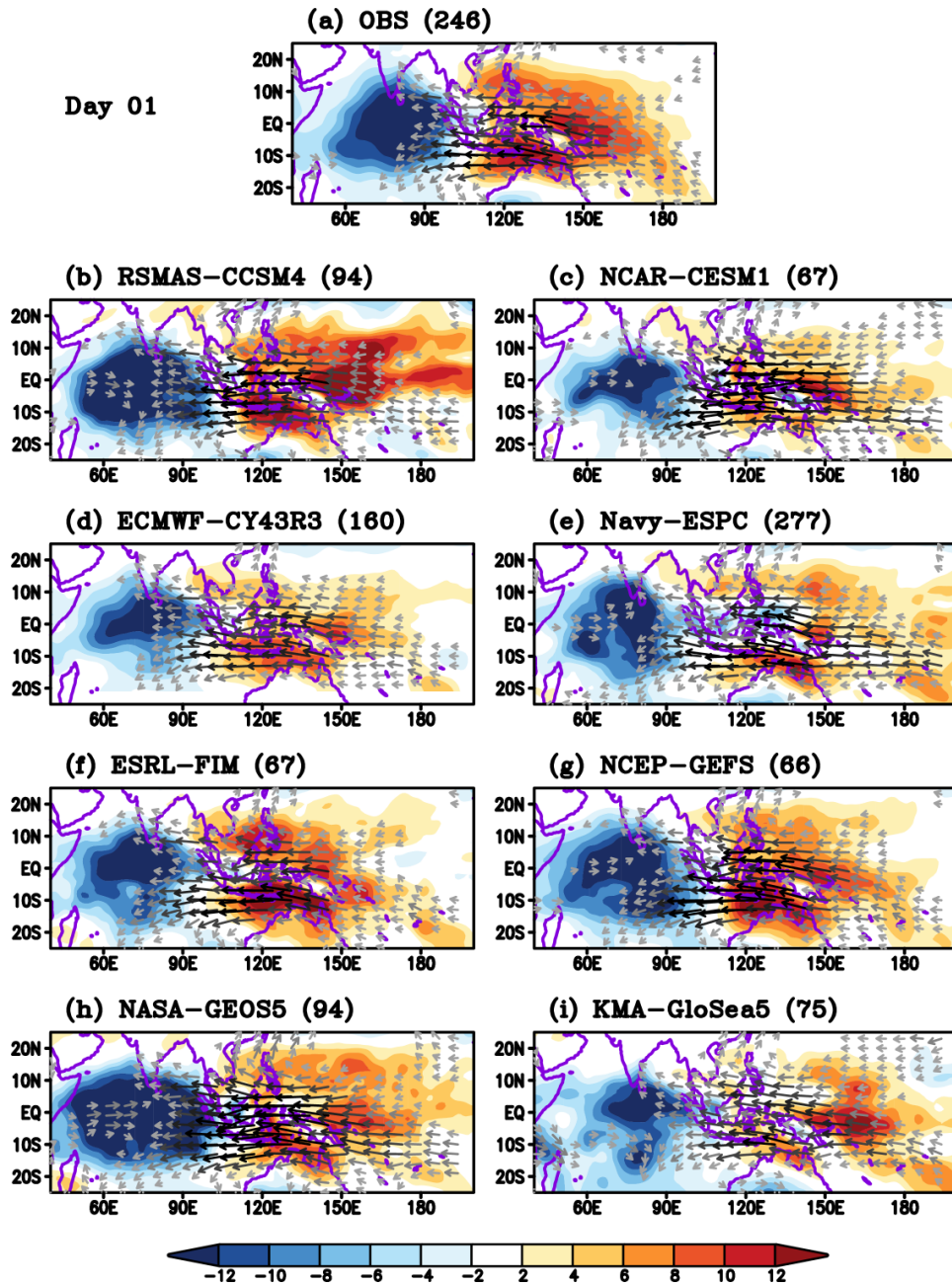
662

663 Figure 2: Same as Figure 1b, except for initial MJO phases. The vertical lines denote forecast

664 lead day-10. Numbers in the parenthesis indicate the number of selected initially strong

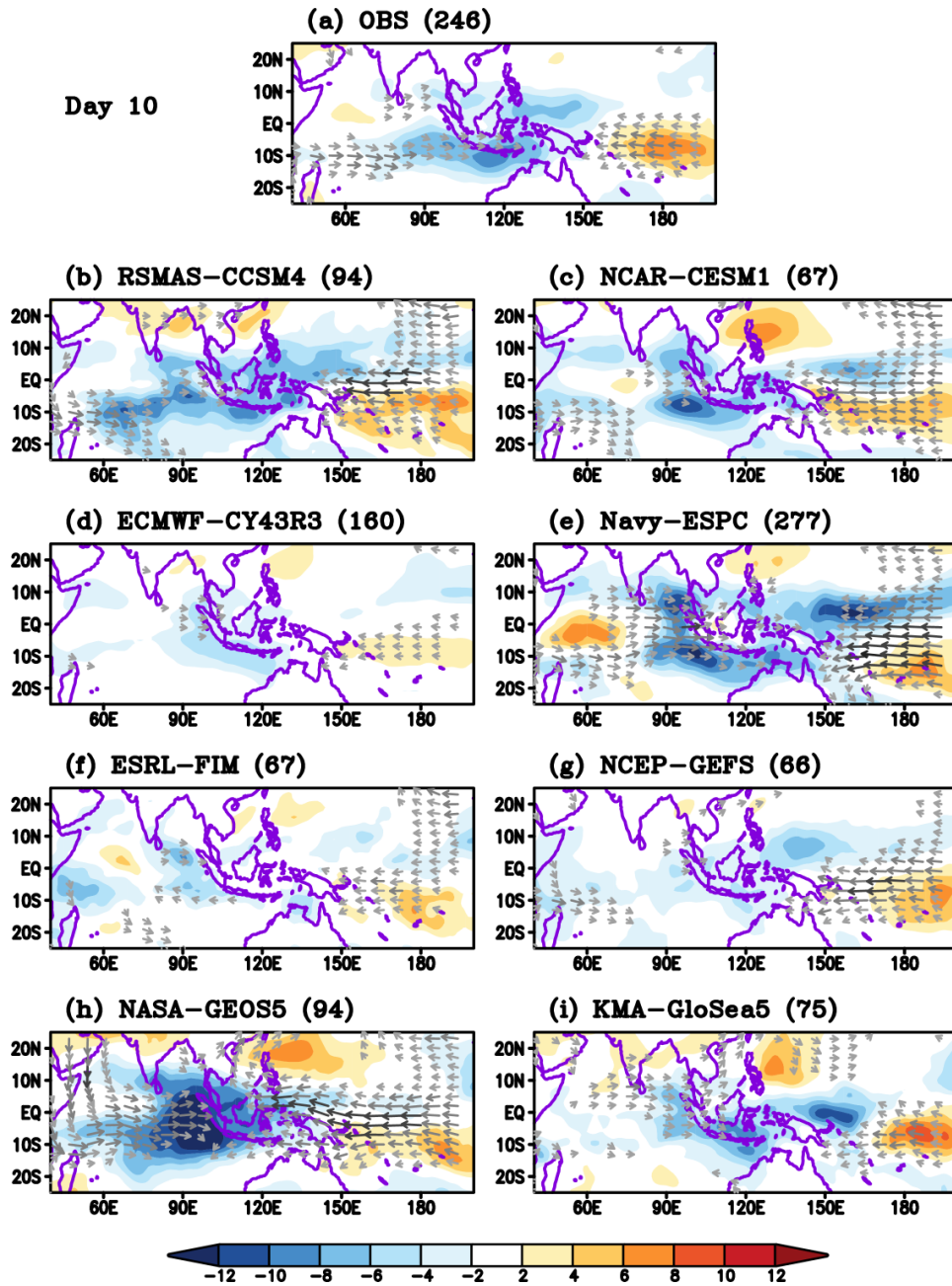
665 MJO events.

666



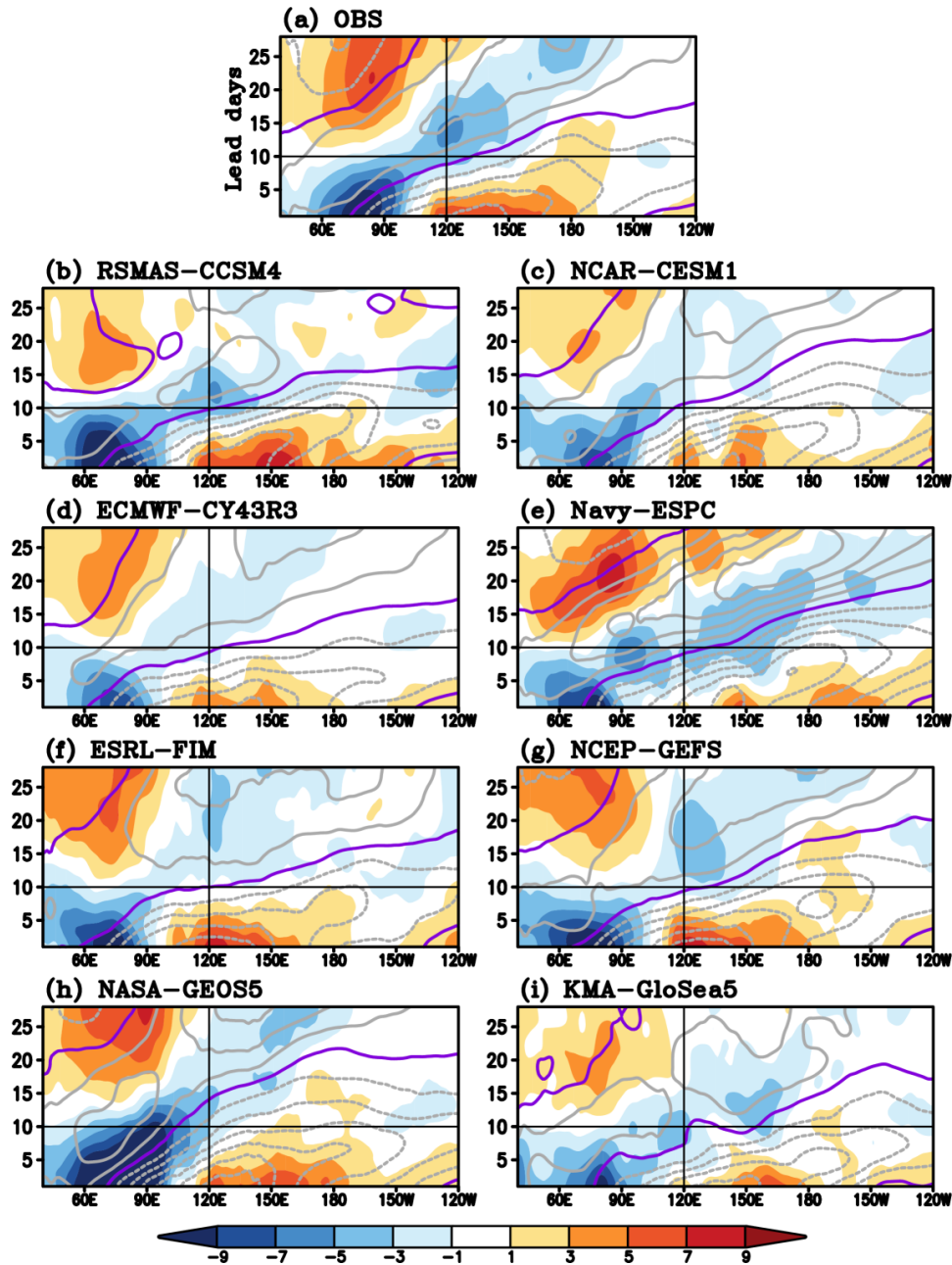
667

668 Figure 3: Day-01 composites of OLR ( $\text{W}/\text{m}^2$ , shading), 850-hPa wind vector, and wind speed  
 669 (m/s, vector colors) anomalies for initially strong MJO events. Numbers in the  
 670 parenthesis indicate the number of selected events. Gray (black) arrow indicates  
 671 windspeed  $> 0.5$  m/s ( $2$  m/s). 5-day moving average and 9-grid-point smoothing are  
 672 applied.



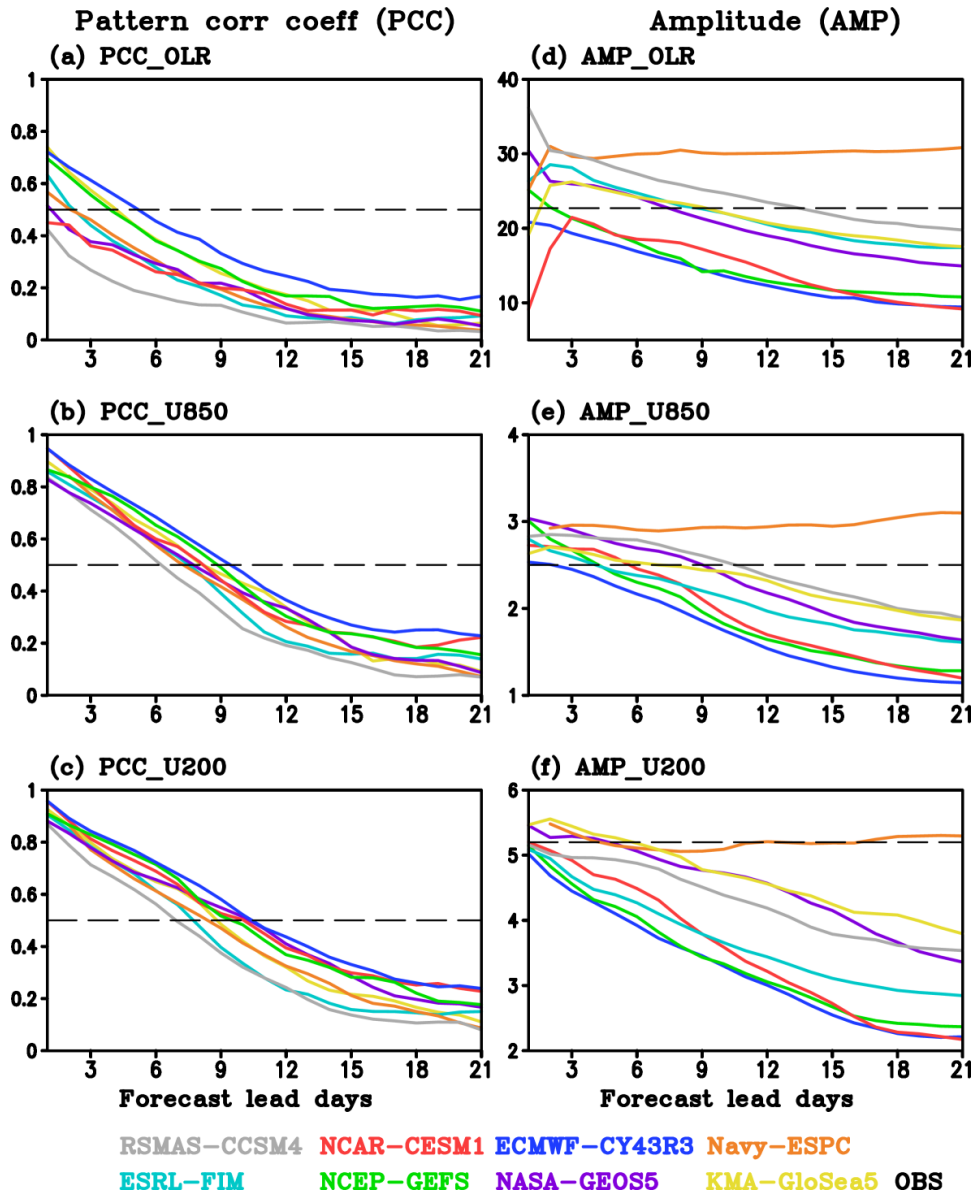
673

674 Figure 4: Same as Figure 3 except for day-10.



675

676 Figure 5: Longitude-time composites of OLR ( $W/m^2$ ; shading) and U850 (contour interval 0.4  
 677 m/s) anomalies averaged over  $20^{\circ}S-20^{\circ}N$  for initially strong MJO events. The purple  
 678 line indicates zero U850 anomalies. The zonal and vertical lines indicate day-10 and  
 679  $120^{\circ}E$  (approximately the center of the MC), respectively. 5-day moving average is  
 680 applied.



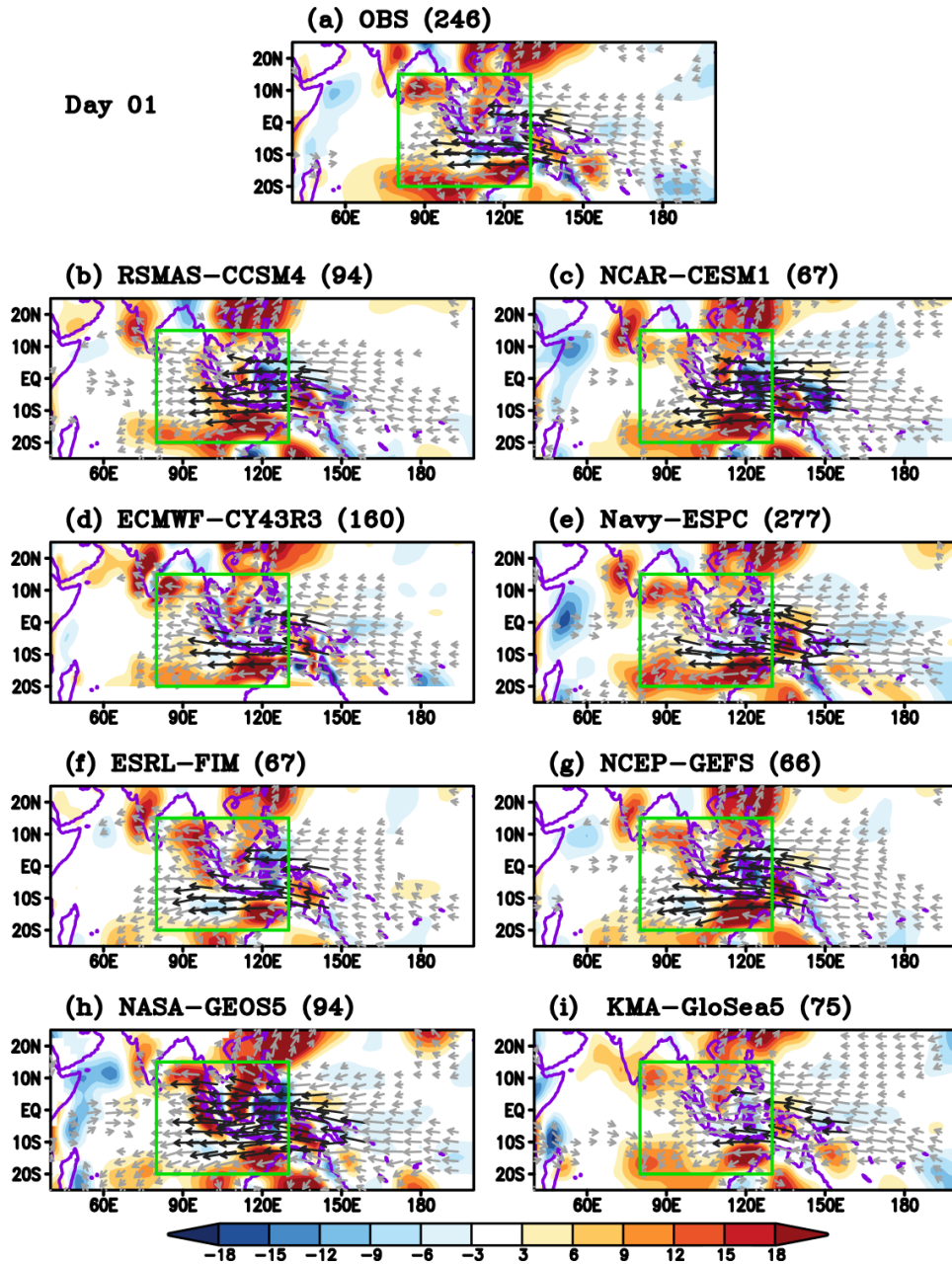
681

682 Figure 6: Mean pattern correlation coefficient (*PCC*) and mean absolute amplitude (*AMP*)

683 calculated over 40°E-200°E and 20°S-20°N as a function of forecast lead days.

684 Horizontal lines indicate (a-c) correlation of 0.5 for *PCC* and (d-f) observed *AMP*. Only

685 initially strong MJO events are selected.

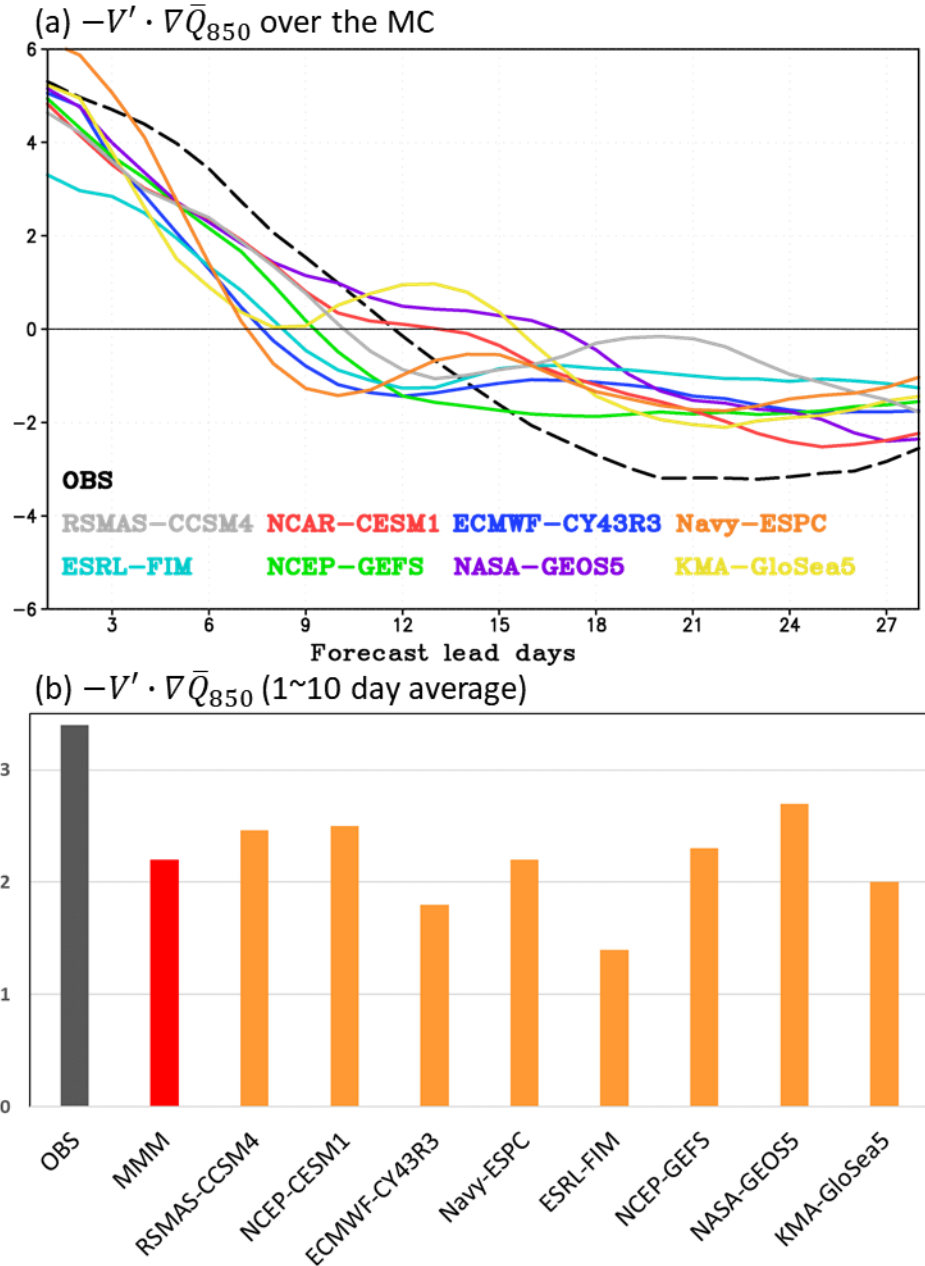


686

687 Figure 7: Same as Fig. 3 except for  $-V' \cdot \nabla \bar{Q}_{850}$  (units:  $10^{-10}/s$ , shading). Green box indicates

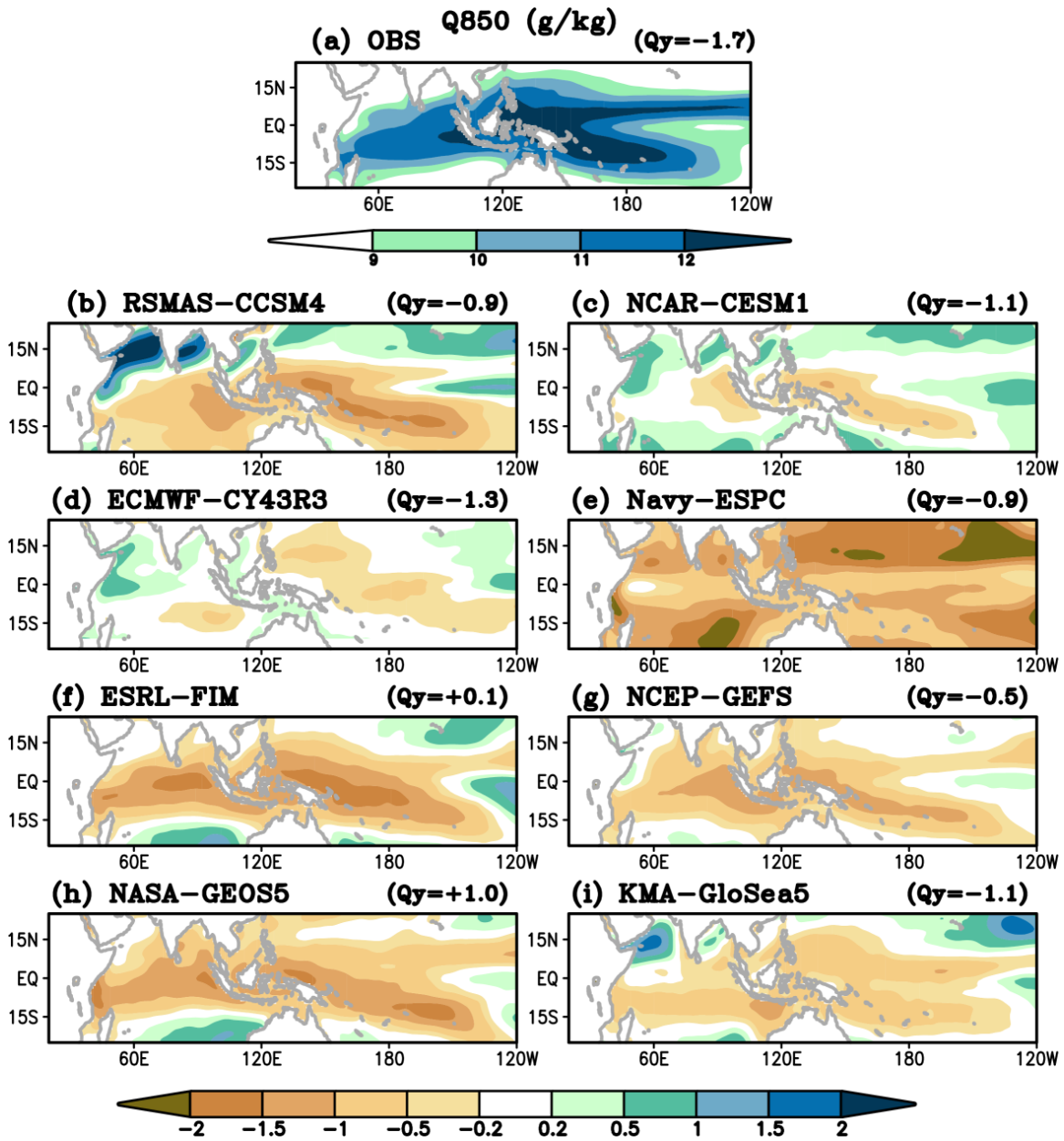
688 the Maritime Continent area ( $80^{\circ}E-130^{\circ}E, 20^{\circ}S-15^{\circ}N$ ). 5-day moving average and 9-

689 grid-point smoothing are applied. Only initially strong MJO events are selected.



690

691 Figure 8: (a) Observed and predicted  $-V' \cdot \nabla \bar{Q}_{850}$  averaged over the MC (green box in Fig. 7) as  
 692 a function of forecast lead days (5-day moving average is applied) and (b) averaged for  
 693 1-10 days. MMM (red bar) denotes the multi-model mean of eight models. Only  
 694 initially strong MJO events are selected.



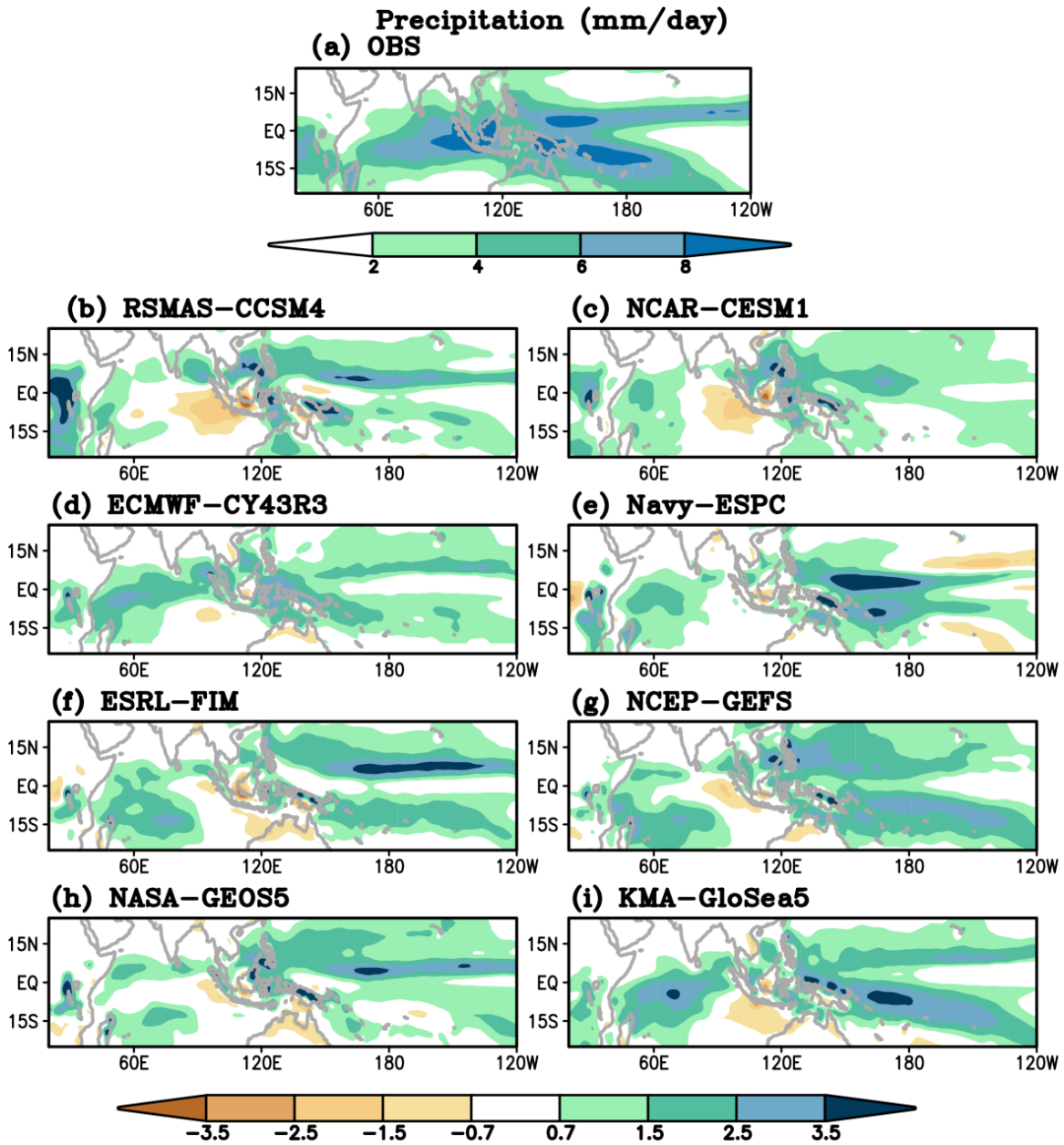
695

696 Figure 9:  $\bar{Q}_{850}$  (g/kg) in (a) observation and (b-h) biases in models. Land area is masked out.

697 Numbers on the top-right indicates the meridional moisture gradient of  $\bar{Q}_{850}$  ( $\bar{Q}_y$ , g/kg)

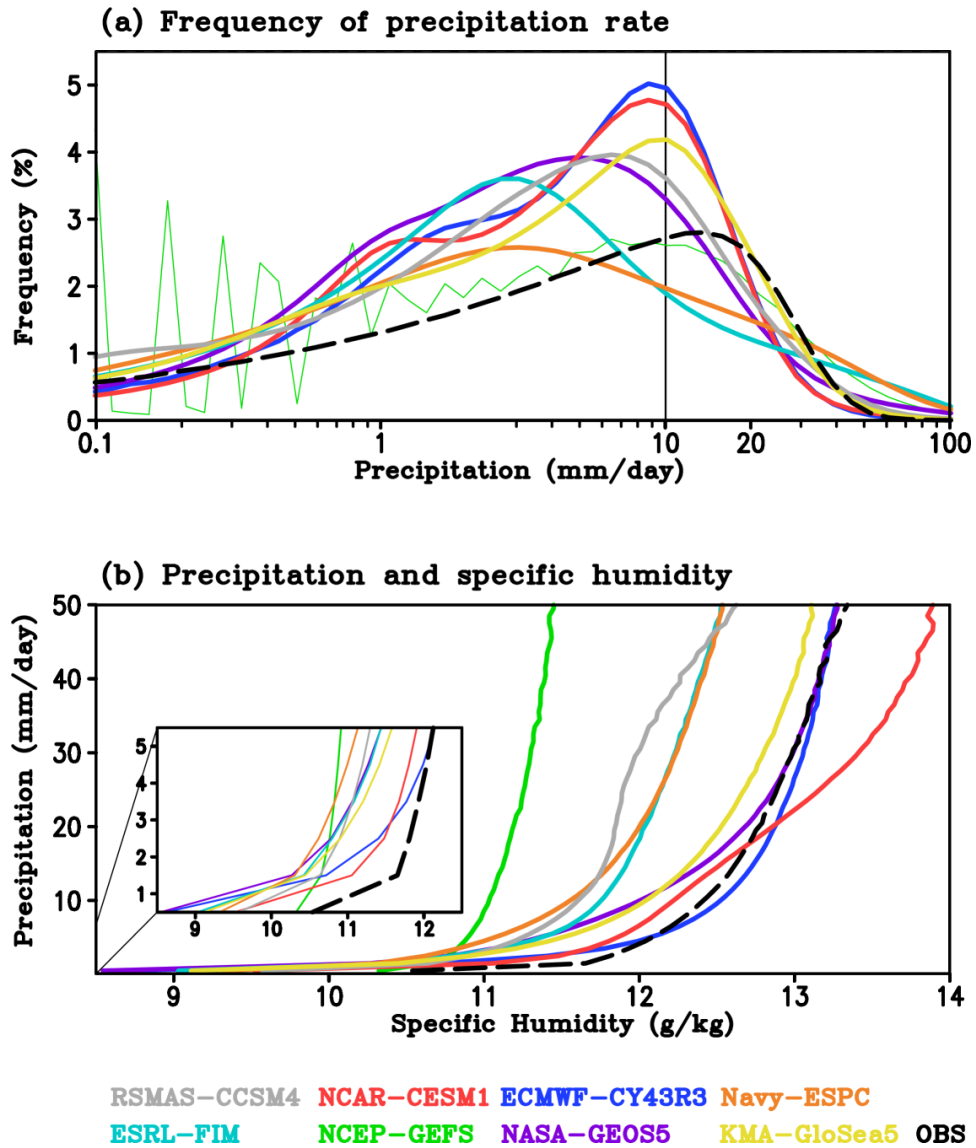
698 defined in the text.

699



700

701 Figure 10: Same as Figure 9, except for precipitation rate (mm/day).



702

703 Figure 11: (a) Occurrence frequency (%) of daily total precipitation rate and (b) distribution of  
 704 daily total precipitation rate in each  $Q_{850}$  bins in observation (GPCP) and reforecasts'  
 705 control simulations averaged over the first 4-weeks over the Indo-Pacific warm pool  
 706 ( $60^{\circ}\text{E}-180^{\circ}\text{E}$ ,  $15^{\circ}\text{S}-15^{\circ}\text{N}$ ). Precipitation is on a log-scale in (a). The black vertical lines  
 707 in (a) indicate precipitation at 10-mm/day.